Examination of the universal behavior of the η-to-π^0 ratio in heavy-ion collisions

Yuanjie Ren ●* and Axel Drees ●†

Department of Physics and Astronomy, Stony Brook University, Stony Brook, New York 11790, USA

We demonstrate that the p_T dependence of the η/π^0 ratio at midrapidity is universal within a few percent for high-energy $p + p$, $p + A$, and $d + A$ collisions, over a broad range of collision energies. The η/π^0 ratio increases with p_T up to 4 to 5 GeV/c where it saturates at a nearly constant value of 0.487 ± 0.024. Above $p_T = 5$ GeV/c, the same constant value is also observed in $A+A$ collisions independent of collision system, energy, and centrality. At lower p_T, where accurate η/π^0 data are absent for $A+A$ collisions, we estimate possible deviations from the universal behavior, which could arise due to the rapid radial hydrodynamic expansion of the $A+A$ collision system. For $A+A$ collisions at the BNL Relativistic Heavy Ion Collider we find that possible deviations are limited to the p_T range from 0.4 to 3 GeV/c and remain less than 20% for the most central collisions.

I. INTRODUCTION

Photons are generally considered ideal probes to study the quark gluon plasma (QGP) created in heavy-ion collisions [1], because they have a long mean free path and leave the collision volume with negligible final-state interactions. Of particular interest are low-momentum or thermal photons with energies of up to several times the temperature of the QGP. The measurement of thermal photons has only recently been possible with the advance of the heavy-ion programs at the BNL Relativistic Heavy Ion Collider (RHIC) [2–4] and the CERN Large Hadron Collider (LHC) [5].

One of the experimental key challenges for these measurements is to estimate and subtract photons from hadron decays that constitute the bulk of photons measured in experiments. The two major contributions of photons result from $\pi^0 \to \gamma + \gamma$ and $\eta \to \gamma + \gamma$ decays. Precise knowledge of the parent π^0 and η p_T spectra is necessary to estimate the decay photon background. While spectra of pions from heavy-ion collisions are well measured at RHIC and LHC, less data exist for η spectra, in particular below p_T of 2 GeV/c. Therefore experiments need to make assumptions how to model the η spectra below 2 GeV/c, which leads to sizable systematic uncertainties. Frequently, experiments have based this extrapolation on the hypothesis of transverse mass m_T scaling of meson spectra [3–5]. However, it has been known since the late 1990s [6] and was recently pointed out again [7] that m_T scaling does not hold below 3 GeV for the η meson.

In this paper we propose a new empirical approach to model the η spectrum that is based on the universality of the η/π^0 ratio across collision systems, beam energies, and centrality selections in heavy-ion collisions. With a good un-

derstanding of the η/π^0 ratio as a function of the transverse momentum p_T and measured π^0 spectra, which are readily available for many collision systems, one can construct a more accurate p_T distribution for η mesons.

The paper is organized as follows. In the next section we elaborate more on the failure of m_T scaling. In Sec. III we discuss two empirical fits and a Gaussian process regression (GPR) to describe the η/π^0 ratio for $p + p$ and $p + A$ collisions, and we document in Sec. IV the universality of η/π^0 across different collision systems ($p + p$, $p + A$, $A+A$), energies, and collision centralities. In Sec. V, we estimate possible deviation from the universal trend at low p_T due to radial flow in heavy-ion collisions. We provide our result for η/π^0 ratios for energies available at RHIC and LHC with systematic uncertainties in the final part.

II. THE FAILURE OF TRANSVERSE MASS SCALING

For measurements of direct photons from heavy-ion collisions, the photons from η and heavier meson decays are frequently estimated using measured π^0 spectra in conjunction with the m_T-scaling hypothesis. A typical implementation of this method [8] starts with a fit to the π^0 spectra with a functional form like a modified Hagedorn function [9]:

$$\frac{1}{2\pi p_T}\frac{d^2N}{dy\,dp_T} = A(M_X)\left(e^{-ag(p_T)-bg(p_T)^2} + \frac{g(p_T, M_X)}{p_0}\right)^{-n},$$

$$(1)$$

with M_X being the meson mass and $g(p_T, M_X) = \sqrt{p_T^2 + m_X^2 - m_\pi^2}$. In this implementation the spectra of the η and heavier mass mesons follow the same distribution with respect to transverse mass $m_T \equiv \sqrt{m^2 + p_T^2}$ as the π^0. The normalization constant $A(M_X)$ is the only free parameter; all other parameters are fixed by the fit to the π^0 data.

*yuanjie@mit.edu
†axel.drees@stonybrook.edu
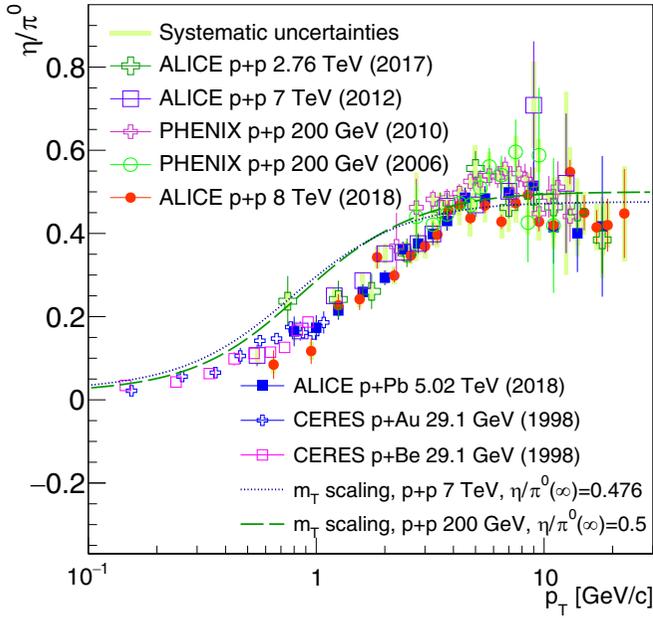
FIG. 1. The η/π^0 ratio of $p + p$ and $p + A$ collisions. Also plotted are the η/π^0 ratios determined by m_T scaling and from a PYTHIA calculation.

FIG. 2. Data for the η/π^0 ratio from $p + p$ and $p + A$ collisions compared to three different methods to describe the data with a universal shape: empirical fit A, empirical fit B, and GPR.

$A(M_X)$ is fitted to experimental data whenever such data exist.

Figure 1 compiles available data of η/π^0 ratios for $p + p$ [10–14] and $p + A$ [6,15] collisions. Also shown in the figure is the result of m_T scaling for two different normalization constants $A(M_\eta)$ [11,12,16] and the expectation from a PYTHIA-6 calculation from Refs. [12,17]. While PYTHIA and the m_T-scaling hypothesis agree well, a significant deviation from the data is seen at low p_T. This was originally discovered at the CERN Super Proton Synchrotron by CERES-TAPS [6] more than 20 years ago and recently confirmed by ALICE at the LHC [10]. Clearly the m_T-scaling hypothesis is not correct and should not be used to extrapolate meson spectra to low p_T for systems where no data exist.

III. DESCRIPTION OF THE η/π^0 RATIOS FOR $p + p$ AND $p + A$ COLLISIONS

The quantitative agreement of the η/π^0 data shown in Fig. 1 is striking, considering the data covers more than 2 orders of magnitude in collision energy. In this section we test different methods to obtain an empirical description of the η/π^0 ratio. The first two methods (A and B) fit a functional shape of the ratio, while the third method (GPR) is a Gaussian process regression that does not assume a specific functional shape. All methods yield similar results below 10 GeV/c; at larger p_T the deviations are sizable and we include these deviations in our evaluation of systematic uncertainties.

A. Empirical fit A

Method A starts with a ratio of two functions of the form given in Eq. (1). The m_T-scaling hypothesis is used to reduce

the number of parameters:

$$R^{\eta/\pi^0}(p_T) = R^\infty \frac{\left(e^{-a \cdot g(p_T) - b \cdot g(p_T)^2} + \frac{g(p_T)}{p_0}\right)^{-n}}{\left(e^{-a p_T - b p_T^2} + \frac{p_T}{p_0}\right)^{-n}}. \quad (2)$$

The advantage of this method is that it preserves a realistic functional form for the p_T spectra with an exponential decrease at low p_T and power law shape at high p_T. In principle, this ensures that at high p_T the η/π^0 ratio approaches a constant value of R^∞. However, unlike starting from the π^0 spectrum, the parameters are fitted to the η/π^0 ratio from $p + p$ and $p + A$ collisions shown in Fig. 1. We achieve a good fit, though the values of the fit parameters are nonphysical and do not describe the individual p_T spectra. The result is depicted in Fig. 2.

The band represents the total uncertainty of the fit function from two sources, the uncertainty of fit parameters, and the systematic uncertainties from data points. The former can be calculated analytically thanks to the explicit fit function, while the latter can be obtained via a "data-shuffling approach" that uses a Monte Carlo technique to vary individual data sets within their systematic uncertainties. This approach is discussed in Appendix B. The total uncertainty shown in the figure represents the quadratic sum of statistical and systematic uncertainties.

B. Empirical fit B

The second empirical fit function has a very similar form, except that normalization of the exponential and power-law component in the numerator are decoupled by introducing an additional parameter. This is implemented such that R^∞

remains the asymptotic value at high p_T:

$$R^{\eta/\pi^0}(p_T) = A \frac{\left(e^{-a \cdot g(p_T) - b \cdot g(p_T)^2} + \left(\frac{R^\infty}{A}\right)^{-\frac{1}{n}} \frac{g(p_T)}{p_0}\right)^{-n}}{\left(e^{-ap_T - bp_T^2} + \frac{p_T}{p_0}\right)^{-n}}. \quad (3)$$

The handling of fit and the calculation of the uncertainties are identical to those in Method A. The result is also shown in Fig. 2. In contrast to Method A, which only gradually approaches the asymptotic value at high p_T, Method B reaches the constant at p_T of about 5 GeV/c and at a lower $R^\infty = 0.487 \pm 0.024$ value, which is used as a reference throughout this article. We note that the change to the constant value is rather abrupt.

C. Gaussian process regression

Both previous methods have a built-in assumption that the η/π^0 ratio has a constant asymptotic value at high p_T. However, the data suggest that there might be a maximum around 8 GeV followed by a decrease towards higher p_T. To avoid any assumptions about the shape, we resort to a machine learning technique called Gaussian process regression (GPR), which possesses no physical knowledge but gives full trust to the data it is given. Details about the GPR can be found in Ref. [18], and comments about the specific implementation we use are summarized in Appendix A. In general, the GPR works best in the region where many consistent data points are available. Less data points or inconsistent data sets lead to larger uncertainties, and unlike the fitting methods the GPR cannot reliably extrapolate much beyond the range covered by the data.

The result of the GPR is presented in Fig. 2, with the band indicating the uncertainties. Over most of the p_T range the GPR gives an equally good description of the data compared to Methods A and B. As expected, it follows the data and peaks near 8 GeV/c. Towards higher p_T, the η/π^0 ratio from the GPR decreases. Whether the drop at high p_T is physical or an artefact of different data sets with different p_T ranges not being perfectly consistent in the range from 3 to 10 GeV/c will only be resolved with more precise data.

Because we do not know the correct functional form of η/π^0, in particular at high p_T, we combine the results obtained with the three methods as our best estimate for a universal η/π^0 ratio for $p + p$ and $p + A$ collisions. This is achieved by assigning every p_T value the minimum of the lower uncertainty range of the three methods as the lower bound and the maximum as the upper bound. The average of the lower and upper bounds is used as the central value. In the following we use $(\eta/\pi^0)_{pp}^{mc}$ to refer to this combined result, with the superscript "mc" referring to maximal coverage of uncertainties. The results are given in Fig. 3 and compared to the m_T-scaling prediction as well as the PYTHIA calculation already shown in Fig. 1. One can see that all of the theoretical predictions overestimate the ratio for p_T below 3–4 GeV/c.

IV. UNIVERSALITY OF η/π^0 RATIO SYSTEMS AT HIGH p_T

In the previous section we established that the η/π^0 ratios measured in $p + p$ and $p + A$ collisions are consistent with
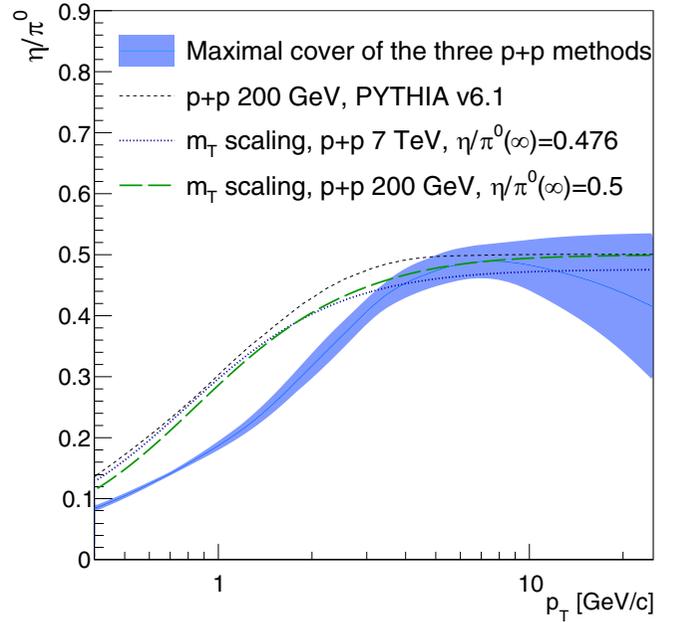
FIG. 3. Result of combining the three empirical methods into one universal estimate of η/π^0 as a function of p_T. Also shown for reference are the estimates based on the m_T-scaling hypothesis and the result of a PYTHIA calculation, both from Fig. 1.

being constant at high p_T with a value of $R^\infty = 0.487 \pm 0.024$ (Sec. III B). Here we demonstrate that all available data from $p + p$, $p + A$, and A+B collisions listed in Table I are consistent with this R^∞ value independent of the collision energy, the collision system, or the collision centrality.

For this demonstration we adopt the functional form from Eq. (3) (empirical fit B). The parameters are fixed using the

TABLE I. References and systems quoted in this article are collected in this table. For each $A+A$ system, if different centralities have different p_T ranges, the one with the minimum bias is presented. All measurements are within less than ± 1 unit around midrapidity.

System	Experiment	$\sqrt{s_{NN}}$	p_T range (GeV/c)	Ref.
$p + p$	CERN WA70	23 GeV	4–6	[19]
$p + p$	Fermilab E706	31.6 GeV	3.25–7.5	[20]
$p + p$	Fermilab E706	38.8 GeV	3.25–9	[20]
$p + p$	PHENIX	200 GeV	2.75–11	[12]
$p + p$	PHENIX	200 GeV	2.25–13	[14]
$p + p$	ALICE	2.76 TeV	0.75–18	[13]
$p + p$	ALICE	7 TeV	0.55–12.5	[11]
$p + p$	ALICE	8 TeV	0.65–22.5	[10]
$p + $Au	CERES-TAPS	29.1 GeV	0.05–1.1	[6]
$p + $Be	CERES-TAPS	29.1 GeV	0.05–1	[6]
$p + $Pb	ALICE	5.02 TeV	0.8–18	[15]
Cu + Au	PHENIX	200 GeV	2.25–19	[21]
$U + U$	PHENIX	192 GeV	2.25–13	[22]
$d + $Au	PHENIX	200 GeV	2.25–11	[12]
Au+Au	PHENIX	200 GeV	2.25–9.5	[12]
Au+Au	PHENIX	200 GeV	5.5–17	[23]
Pb+Pb	ALICE	2.76 TeV	1.25–18.5	[24]
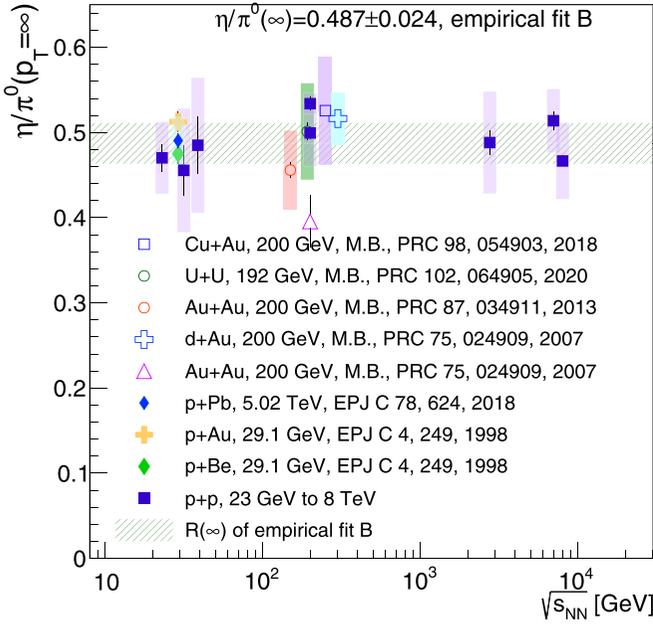
FIG. 4. Values of $R^\infty = \eta/\pi^0(p_T \to \infty)$ as a function of $\sqrt{s_{NN}}$ for the minimum bias $p + p$, $p + A$, and A+B data sets. Statistical errors are shown as bars, and systematic uncertainties are shown as bands. Also shown is a band representing 0.487 ± 0.024, the result of the empirical fit B to the combined $p + p$ and $p + A$ data. Note that the A+B data at 200 GeV are offset in $\sqrt{s_{NN}}$ to avoid overlap of data sets.

simultaneous fit to the $p + p$ and $p + A$ data to the following values: $a = -1.24$, $b = 0.482$, $p_0 = 4.15$, $n = 5.07$, and the composite parameter $R^\infty/A = 2.28$. The final fit parameter R^∞ is determined individually for each data set using the data-shuffling method. For each data set we vary the points many times within their systematic uncertainties, as discussed in Appendix B, and create an ensemble of R^∞ and $\sigma_{R\infty}$ values. The mean of the R^∞ ensemble is used as the measurement of R^∞ for the η/π^0 ratio and the standard deviation is quoted as the systematic uncertainty. The mean of the $\sigma_{R\infty}$ ensemble is quoted as the statistical uncertainty.

Figure 4 shows the results as a function of the nucleon-nucleon center-of-mass energy $\sqrt{s_{NN}}$ for the minimum bias data samples of all collision systems. Also shown in the figure is the R^∞ value obtained from the combined fit to the $p + p$ and $p + A$ data sets using method B. Within uncertainties, all data sets are consistent with this value and there is no evidence for a $\sqrt{s_{NN}}$ dependence of R^∞.

For most publications of η/π^0 ratios from heavy-ion collisions, the data were also presented for centrality selected event classes. To include these in the comparison, we plot R^∞ as a function of the number of the produced particle $dN_{\text{ch}}/d\eta|_{\eta=0}$. The $dN_{\text{ch}}/d\eta$ values used are summarized in Table II. The results are given in Fig. 5. Again all values are consistent with a universal value within uncertainties. This analysis strongly suggests that R^∞ does not depend on the collision systems, $\sqrt{s_{NN}}$, or the centrality of the collisions.

Recent measurements of direct photon emission in heavy-ion collisions have used a value of $\eta/\pi^0 = 0.46 \pm 0.06$ at

TABLE II. Values for $dN_{\text{ch}}/d\eta$ at midrapidity for all collision systems and centrality selections used in this work. For $p + p$ collisions, the numbers correspond to the inelastic $p + p$ cross section as given in Ref. [25]. For all other cases, whenever a reference is given, the values are taken directly from the publication. For PHENIX data we use data tabulated in Ref. [26]. The symbol * in the reference indicates that the value was extrapolated beyond what was tabulated. All minimum bias values (MB) that are marked by ** were calculated from the centrality selected data sets for the same system. For all data the uncertainties were calculated assuming that the values quoted in the reference are fully correlated. Reference [6] does not give an uncertainty on the multiplicity value.

System	$\sqrt{s_{NN}}$	Centrality	$dN_{\text{ch}}/d\eta$	Ref.
$p + p$	$\sqrt{s}$	—	$\alpha(\sqrt{s}/\text{GeV})^{2\delta}$	[25]
$p + Au$	29.1 GeV	—	4.7	[6]
$p + Be$	29.1 GeV	—	3.0	[6]
$p + Pb$	5.02 TeV	—	16.8 ± 0.7	[27]
$d + Au$	200 GeV	0%–20%	17.4 ± 1.2	[26]
		20%–40%	12.2 ± 0.9	[26]
		40%–60%	8.4 ± 0.6	[26]
		60%–88%	1.7 ± 0.4	*
		MB	9.2 ± 0.8	**
Cu + Au	200 GeV	0%–20%	268 ± 20	[26]
		20%–40%	131 ± 10	[26]
		40%–60%	54 ± 4	[26]
		60%–93%	12.2 ± 1.5	*
		MB	102 ± 9	**
Au+Au	200 GeV	0%–20%	519 ± 26	[26]
		20%–60%	156 ± 11	[26]
		60%–92%	16.5 ± 2	*
		MB	186 ± 11	**
$U + U$	192 GeV	0%–20%	636 ± 51	[26]
		20%–40%	268 ± 21	[26]
		40%–60%	79 ± 8	*
		60%–80%	18.6 ± 3	*
		MB	234 ± 35	**
Pb+Pb	2.76 TeV	0%–10%	1448 ± 55	[28]
		20%–50%	445.3 ± 10	[28]

a p_T of 5 GeV/c with an uncertainty of about 13% [3,5]. The quoted uncertainty accommodates the significant variations between different measurements at energies available at RHIC. We propose that the apparent differences are likely due to systematic effects specific to individual data sets, rather than due to physical differences. Thus using a universal value for R^∞ can reduce the uncertainties by a factor of 2 to 3 to 5% for all collision systems.

V. THE EFFECT OF RADIAL FLOW

We have shown that the η/π^0 ratio can be described by one common function for all $p + p$ and $p + A$ collisions over the measured p_T range from 0.1 to 20 GeV/c. Furthermore, above $p_T = 5$ GeV/c, the same function describes all data from heavy-ion collisions. Whether this universal function also describes heavy-ion data at lower p_T cannot be tested due to the absence of accurate experimental data. However, there
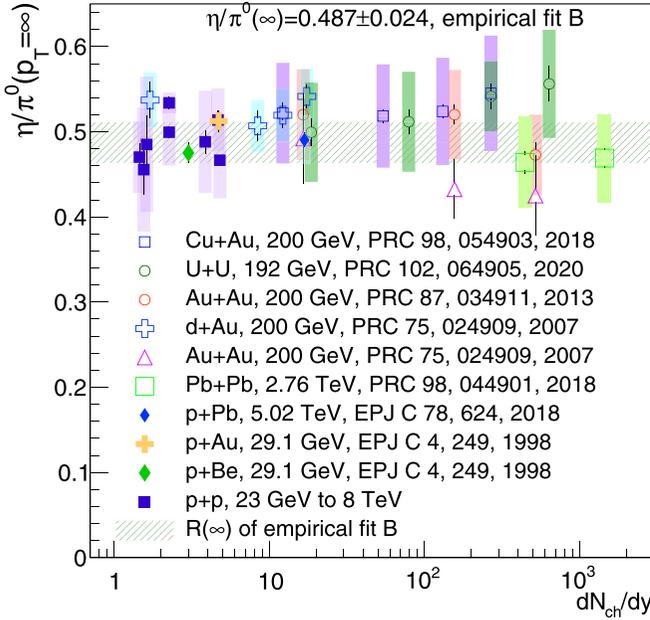
FIG. 5. Values of $R^\infty = \eta/\pi^0(p_T \to \infty)$ as a function of $dN_{ch}/d\eta$. The presentation is identical to Fig. 4; however, for A+B collisions results from different centrality classes are shown rather than results for the minimum bias sample.

FIG. 6. Schematic comparison of π, K, and p spectra from Au+Au and $p + p$ collisions at $\sqrt{s_{NN}} = 200$ GeV. All spectra are approximately normalized to their rapidity density at midrapidity. Different particle types are separated by factors of 10 for clarity.

are reasons to believe that this universality does not hold at low p_T.

Evidence for strong collective motion of the bulk of the produced particles has been observed in all high-energy heavy-ion collisions. This motion is consistent with a Hubble-like hydrodynamic expansion of the collision volume, with a linear velocity profile in the radial direction. In this velocity profile, heavier particles gain more momentum than lighter ones. Radial flow effectively depletes the particle yields at low p_T and enhances them in an intermediate-p_T range, which is determined by the mass of the particle. For p_T values much larger than the particle's mass, radial flow becomes negligible. Figure 6 shows the effect schematically by comparing π, K, and p spectra at energies available at RHIC. The spectra shown are roughly to scale and consistent with experimental data from 200-GeV Au+Au collisions. They are normalized per particle of the corresponding type at midrapidity.

Because the η meson has about the same mass as the kaon, one would expect that in the momentum range from a few hundred MeV/c to a few GeV/c radial flow would increase the yield of η mesons significantly more than that of π^0. This in turn would increase the η/π^0 ratio in heavy-ion collisions compared to that observed in $p + p$ and $p + A$ collisions.

To quantify the size of the modification due to radial flow, we use a double ratio R_{flow} defined as follows:

$$R_{\text{flow}} \equiv \frac{\left(\frac{\eta}{\pi^0}\right)_{C_i}}{\left(\frac{\eta}{\pi^0}\right)_{p+p}} \approx \frac{\left(\frac{K^\pm}{\pi^\pm}\right)_{C_i}}{\left(\frac{K^\pm}{\pi^\pm}\right)_{p+p}} \equiv \frac{\left(R_{AA}^{K^\pm}\right)_{C_i}}{\left(R_{AA}^{\pi^\pm}\right)_{C_i}}, \qquad (4)$$

where we take advantage of the fact the momentum boost from radial flow is mostly determined by the particle mass and that $m_{K^\pm} \approx m_\eta$. Also, charged pions are used instead of

neutral pions, because $\pi^\pm$ and kaons are typically measured simultaneously with the same detector systems and, thus, most systematic uncertainties on the measurement cancel in the double ratio. The subscript C_i refers to a specific collision system, energy, and centrality selection.

Figure 7 presents R_{flow} for different centrality classes of Au+Au collisions at 200 GeV. The values were calculated from data published by PHENIX [29]. The data cover the p_T range from 0.5 to 2 GeV/c and the GPR is used to extrapolate somewhat beyond the measured range. According to this estimate, the η/π^0 ratio is enhanced in central collisions in a p_T region from 0.4 to 3 GeV/c with a maximum of about 25% near 1 GeV/c. The enhancement is reduced for more peripheral collisions and nearly vanishes for the 60%–92% selection.

In Fig. 8 we depict the estimate for R_{flow} for Pb+Pb data at 2.76 TeV calculated from K and $\pi^\pm$ data measured by ALICE [24,30]. Shown are results for a 0%–10% centrality selection. Only statistical uncertainties are shown. The flow effect is significantly larger at LHC than at RHIC: the p_T range affected is extended to 5–6 GeV/c, it reaches its maximum at higher p_T around 3 GeV/c, and the maximum has increased to about 50%. All this indicates that radial flow effects increase with beam energy, which is consistent with a higher initial pressure and a longer lifetime of the system at the LHC compared to the RHIC.

ALICE also has published η/π^0 ratios for Pb+Pb collisions at 2.76 TeV [24] down to 1 GeV/c, which can be used
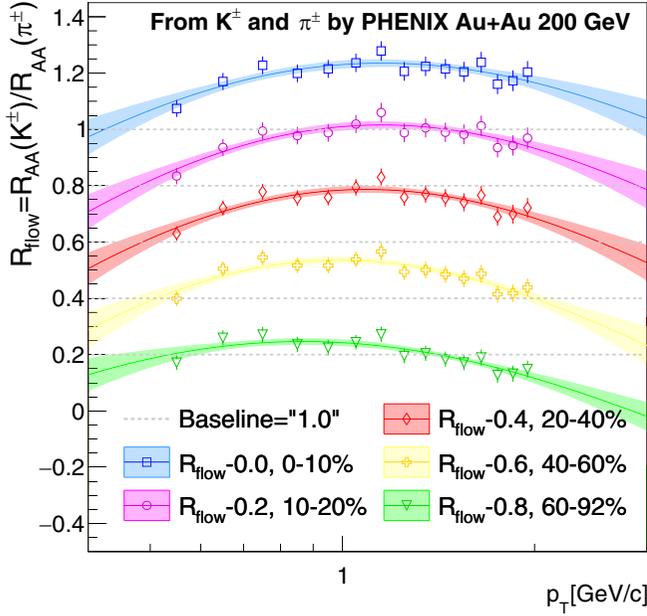
FIG. 7. Double ratio, obtained by $(R^K_{AA})_{C_i}/(R^\pi_{AA})_{C_i}$.

to verify the validity of the R_{flow} estimate from K/π. For this we have divided Pb+Pb data by the universal $(\eta/\pi^0)^{\text{mc}}_{pp}$ from Fig. 3. The results are also shown in Fig. 8; error bars represent the combined uncertainty of $(\eta/\pi^0)^{\text{mc}}_{pp}$ and the statistical uncertainty of $(\eta/\pi^0)_{\text{PbPb}}$. The ansatz that

$$\frac{(K^\pm/\pi^\pm)_{\text{cent}}}{(K^\pm/\pi^\pm)_{pp}} \approx \frac{(\eta/\pi^0)_{\text{cent}}}{(\eta/\pi^0)_{pp}}$$

is consistent with the data.
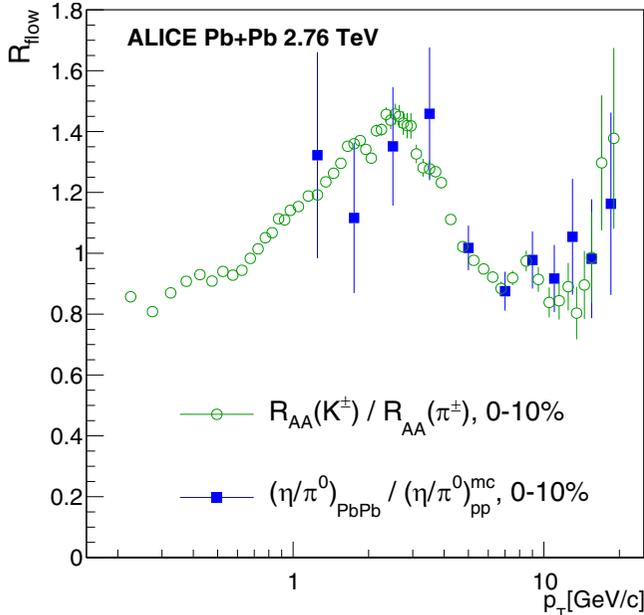
FIG. 8. Double ratio (the flow ratio) for $K^\pm/\pi^\pm$ and η/π^0 in Pb+Pb collisions at 2.76 TeV.

To construct an η/π^0 ratio for a specific collision system and centrality selection, we modify the universal shape $(\eta/\pi^0)^{\text{mc}}$ determined from $p+p$ and $p+A$ data (see Fig. 3 from Sec. III) with R_{flow} for the selected heavy-ion sample:

$$\left(\frac{\eta}{\pi^0}\right)_{C_i} = \left(\frac{\eta}{\pi^0}\right)_{pp} R_{\text{flow}} \approx \left(\frac{\eta}{\pi^0}\right)_{pp} \frac{\left(\frac{K^\pm}{\pi^\pm}\right)_{C_i}}{\left(\frac{K^\pm}{\pi^\pm}\right)_{pp}}. \quad (5)$$

Because R_{flow} may be available only in a limited p_T region, for example, from 0.4 to 2 GeV/c in Fig. 7, we propose the following procedure that can be applied to any A+B collisions system if $\pi^\pm$ and K data are available for the p_T range affected by the radial flow. In the first step we create pseudo data for η/π^0 by multiplying R_{flow} point-by-point with the $(\eta/\pi^0)^{\text{mc}}_{pp}$ up to p^{cut}_T where $R_{\text{flow}}(p_T) \approx 1$. This range extends to 1.4 or 4.5 GeV/c for Au+Au at 200 GeV at 60%–92% centrality and Pb+Pb at 2.76 TeV, respectively. To ensure that our flow estimate has the correct asymptotic behavior we add a second set of pseudo data with constant values of $\eta/\pi^0 = 0.487 \pm 0.024$. These are added either above 4 GeV/c where all data sets can be described by a constant (see Sec. IV) or above $1.6 \times p^{\text{cut}}_T$, whichever is larger. The combined pseudo data are processed through a GPR to obtain a smooth curve. Finally, to account appropriately for the systematic uncertainties at high p_T we merge the GPR describing the flow effect with $(\eta/\pi^0)^{\text{mc}}_{pp}$ above p^{cut}_T. The uncertainty band at low p_T is also taken to be whichever is larger.

In Fig. 9 the construction η/π^0 is presented step by step for three examples: 0%–20% and 60%–92% Au+Au at 200 GeV and 0%–10% Pb+Pb at 2.76 TeV, in panels (a) to (c), respectively. The pseudo data generated are represented by points, which are then processed through a GPR resulting in the hashed green bands. They are contrasted with $(\eta/\pi^0)^{\text{mc}}_{pp}$, the blue band, and merged with it above p^{cut}_T to create the final green envelope representing our η/π^0 estimates. As discussed above, the largest flow effect is observed for central Pb+Pb collisions at the LHC [Fig. 9(c)]. For central Au+Au collisions at the RHIC [Fig. 9(a)], a much smaller effect is observed, and finally peripheral collisions of the same system are consistent with no flow effect [Fig. 9(b)].

These best estimates are compared to data in Fig. 10. For the comparison we selected data sets with similar charged-particle densities, so that despite the difference in collision systems, centrality or $\sqrt{s_{NN}}$ matter was created under similar conditions and evolved the same way with time. In all three cases our best estimates are consistent with the η/π^0 data.

VI. SUMMARY DISCUSSION

We find a universal p_T dependence of η/π^0 for all $p+p$ and $p+A$ collisions independent of the center-of-mass energy from $\sqrt{s_{NN}} = 23$ GeV to 8 TeV. We note that, like originally discovered in Ref. [6], below 3 GeV/c the universal ratio is significantly below m_T-scaling extrapolations from higher p_T.

That there is no $\sqrt{s_{NN}}$ dependence is surprising because the p_T spectra of all particles vary strongly with $\sqrt{s_{NN}}$ and particle production from jet fragmentation becomes increasingly prevalent at higher energies. None-the-less there seems to be no impact on the relative yield at which η and π^0 are
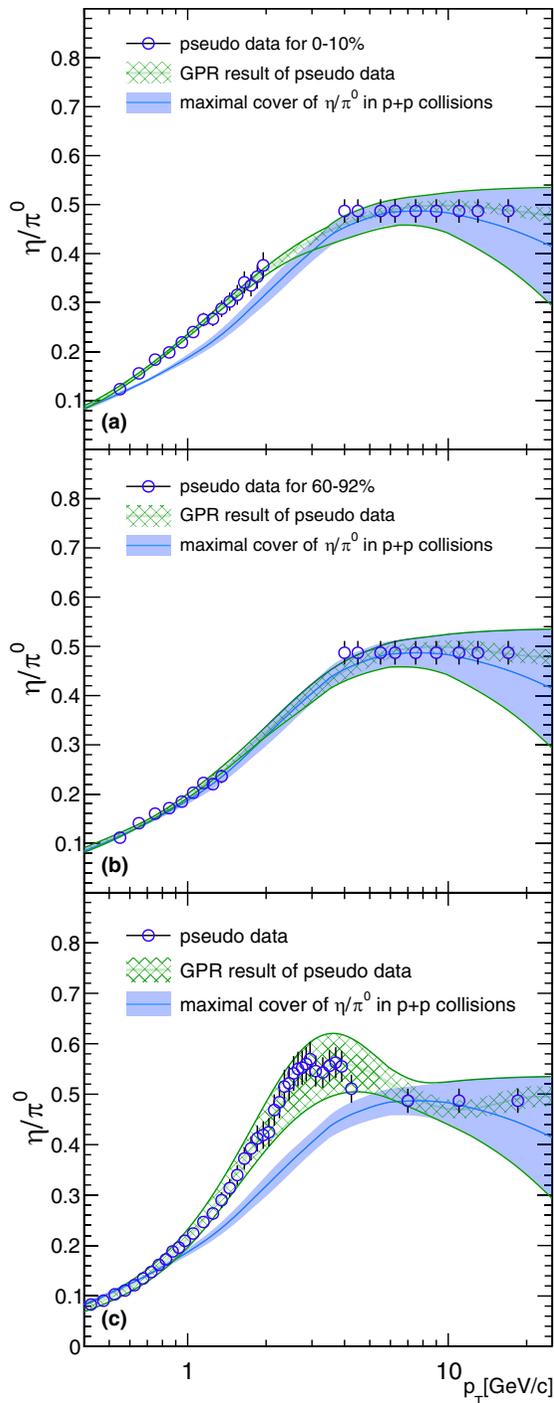
FIG. 9. Estimate of the effect of radial flow on η/π^0 for 0%–20% and 60%–92% Au+Au collisions at 200 GeV and 0%–10% Pb+Pb collisions at 2.76 TeV. Details are discussed in the text.

FIG. 10. Estimate of the effect of radial flow on η/π^0 for 0%–20% and 60%–92% Au+Au collisions at 200 GeV and 0%–10% Pb+Pb collisions at 2.76 TeV. Data sets of comparable systems are also shown. Details are discussed in the text.

produced. This may hint at a largely universal hadronization process in which hadrons are always created under the same conditions, even if the underlying mechanism is considered different, for example, bulk particle production or jet fragmentation.

For heavy-ion collisions, η/π^0 ratios have the same universal behavior at high p_T, independent of collision species,

collision energy, or collision centrality. For lower p_T we find evidence for modifications of the relative particle yields due to radial flow. One might speculate that the same universal harmonization process is at work but that hadrons are produced in a moving reference frame.
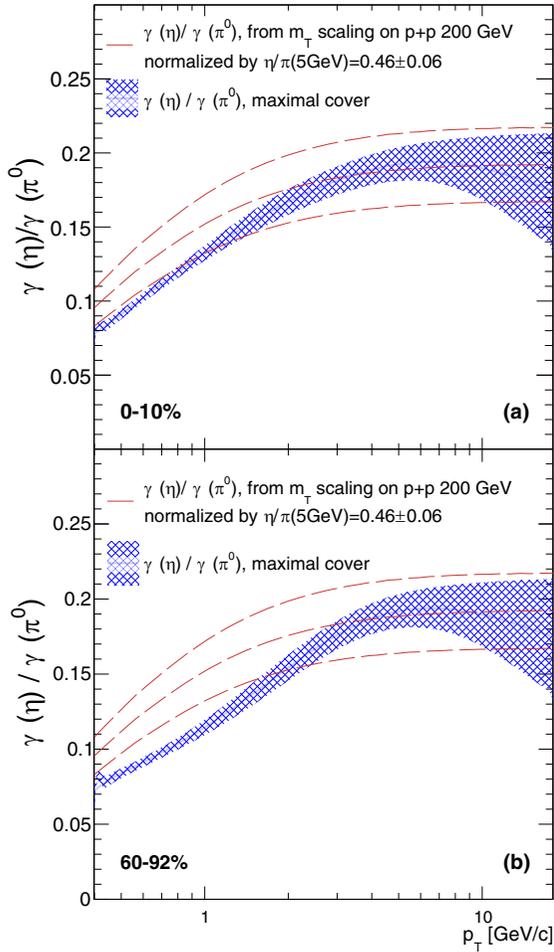
FIG. 11. Ratio of photons from the decay of the two mesons. The grid band corresponds to the η/π ratio in Fig. 10. The dashed line corresponds to the distribution of η using the m_T-scaling method by fitting with the data of $p + p$ at 200 GeV.

We have quantified the modification of the η/π^0 ratio due to radial flow using the double ratio $R_{AA}(K)/R_{AA}(\pi)$. This assumes that the change of the p_T spectra depends entirely on the particle mass, but it does not make any assumptions about the similarity of η and kaon spectra themselves. We note that our approach may overestimate the modification due to flow, since kaon production or generally strange quark production is enhanced in heavy-ion collisions. In our estimate the modification increases with $\sqrt{s_{NN}}$. At 200 GeV at the RHIC the maximum increase of η/π^0 is estimated to be 25% around 1 GeV/c; in contrast, at 2.76 TeV at the LHC the maximum increase is nearly 50% and occurs at higher p_T between 2 and 3 GeV/c.

With our original motivation in mind, which was to reduce systematic uncertainties on the measurement of direct photons, we proposed a new methodology to create η/π^0 ratios. This method is more accurate than frequently used extrapolations to lower p_T based on m_T scaling and does not suffer from the frequent lack of statistics for η measurements. Our approach can be applied to all systems for which $K/\pi^{\pm}$ is measured in the p_T range affected by radial flow. The

method does not require actual measurements of η production for a given system. We have tested this method for two specific collision systems. In Fig. 11 we show the ratio of photons from decays of η mesons to those from π^0 decays for Au + Au collisions at 200 GeV. Figure 11(a) shows central collisions and Fig. 11(b) shows a peripheral event selection. Both panels compare the results of our method to what has been most recently used by the PHENIX Collaboration in direct photon analyses [3,4]. The number of photons from η decays are negligible at low p_T, but increase to about 20% at high p_T. This reflects the η/π^0 ratio of about 0.5 and the smaller branching ratio of approximately 40% of the η decay to two photons. The uncertainty band is given by the 2.2% uncertainty quoted by PHENIX, which results from the assigned error on $\eta/\pi(5 \text{ GeV}) = 0.46 \pm 0.06$ and some contribution at lower p_T due to the m_T-scaling assumption. The uncertainty on the photon contribution from η relative to that of π^0 is the third largest individual contribution to the systematic uncertainties on their direct photon measurement. The improvement from our method is clearly visible. In the range from 2 to 6 GeV/c the systematic errors are reduced by at least a factor of 2, and for lower momenta the reduction is even larger. With this improvement, the systematic error on the decay photon contribution from the η meson becomes negligible.

As noted earlier, the m_T-scaling assumptions overestimate the contribution from η at low p_T, and as a consequence the direct photon yield below 2 GeV was slightly underestimated. For central Au+Au collisions at 200 GeV, the effect is within the quoted systematic uncertainties, which is due to a partial compensation by the effect of radial flow. For central Pb+Pb collisions at 2.76 TeV, the flow modifications are larger and coincidentally bring η/π^0 much closer to the m_T-scaling assumption used in the measurement of direct photons published by ALICE [5].

APPENDIX A: GAUSSIAN PROCESS REGRESSION

In this section we discuss the implementation of the Gaussian process regression (GPR) used in our analysis. Full details about the GPR can be found in Ref. [18]. We start with a selection of N data points: x_i, y_i, and σ_i^2. In our case this is typically N values of $\log 10(p_T)$ and $\eta/\pi^0(p_T)$ and its variance. We use a square-exponential (SE) kernel to describe the correlation between points, which is given by

$$k_{\text{SE}}(x_i, x_j) = \sigma_p^2 \exp\left(-\frac{(x_i - x_j)^2}{2l^2}\right). \quad \text{(A1)}$$

Here σ_p gives the strength of the correlation between y values and l is a length scale that determines the range in x over which y values are correlated.

We introduce the vectors X and Y, which have dimension N and elements x_i and y_i, i.e., the data. The correlations between

y values is then defined by the covariance matrix K_{xx}, which has the elements

$$(K_{xx})_{ij} = k_{SE}(x_i, x_j) + \delta_{ij}\sigma_i^2, \tag{A2}$$

with $\delta_{ii} = 1$ and $\delta_{ij} = 0$ for $i \neq j$. The term $\delta_{ij}\sigma_i^2$ adds noise to the diagonal elements to account for the uncertainty on the measured y values. To determine σ_p and l, we maximize the log likelihood function:

$$\log p(Y|\sigma_p, l) = -\frac{n}{2}\log 2\pi - \frac{1}{2}Y^T[K_{xx}]^{-1}Y$$
$$- \frac{1}{2}\log\det(K_{xx}). \tag{A3}$$

Once the parameters σ_p and l are set, we can predict y values for any given x value. For this we introduce vectors X^* and Y^* of dimension R and elements x_i^* for which we want to predict y_i^*, with R typically much larger than N. We introduce two more matrices, one of dimension $R \times N$ with elements $(K_{x^*x})_{ij} \equiv k_{SE}(x_i^*, x_j)$ and one of dimension $R \times R$ with elements $(K_{x^*x^*})_{ij} \equiv k_{SE}(x_i^*, x_j^*)$. The predicted values Y^* and their covariance matrix $\mathrm{Cov}(Y^*)$ are then calculated as follows:

$$Y^* = K_{x^*x}[K_{xx}]^{-1}Y, \tag{A4}$$

$$\mathrm{Cov}(Y^*) = K_{x^*x^*} - K_{x^*x}[K_{xx}]^{-1}K_{x^*x}^T. \tag{A5}$$

The diagonal elements of $\mathrm{Cov}(Y)$ give the variance of Y^* due to the statistical uncertainty on the data Y. We refer to this as vector S_{stat}^*. We also consider the fit uncertainty on σ_p and l. The variance can be calculated by the covariance matrix M the fitting procedure provides through error propagation of Eq. (A4):

$$S_{fit} = (\partial_l y^*)^2 M_{ll} + 2\partial_l y^* \partial_{\sigma_p} y^* M_{l\sigma_p} + (\partial_{\sigma_p} y^*)^2 M_{\sigma_p\sigma_p},$$
$$\forall \ y^* \in Y^*, \tag{A6}$$

with ∂_l and ∂_{σ_f} being the partial derivatives of Y^* with respect to l and σ_p.

In addition, we incorporate the systematic uncertainties using the data-shuffling method discussed in Appendix B.

We create a large ensemble of different $\{Y_\lambda^*\}$ for the same X^* by varying each data set by a Gaussian random number $\epsilon \sim N(0, 1)$, multiplying systematic uncertainties. The pointwise variance of ensembles $\{Y_\lambda^*\}$, which we call S_{Sys}^*, is used as measure of the systematic uncertainty.

In all figures that show results from the GPR the center line represents Y^* and the vertical width of the band is $\sqrt{S_{stat} + S_{fit} + S_{Sys}^*}$, pointwise.

APPENDIX B: DATA-SHUFFLING METHOD

The *data-shuffling method* is a Monte Carlo simulation approach that allows one to estimate the effect of systematic uncertainties on the result of a fit of a function to data. To illustrate how the method works we first consider the case of one data set and assume that the systematic uncertainties are fully correlated. Here fully correlated means that the correlation matrix is $\rho_{ij} = 1, \forall i, j$. Suppose each data point is described by a 4-tuple $(x_i, y_i, \sigma_i^{stat}, \sigma_i^{sys})$. One first defines a Gaussian random variable $\epsilon \sim N(0, 1)$. In each simulation, one shifts each y by a small quantity to $y_i' = y_i + \sigma_i^{sys}\epsilon$ accordingly. Then in each simulation, one fits with these shifted data and gets one fit result. This is repeated L times, which generates L sets of fit parameters. For each set of fit parameters one can divide the x values into R bins. Both L and R are usually large numbers. This results in an L-by-R matrix of $y_{\lambda r}$ values. For a fixed r, the mean and the standard deviation of $\{y_{\lambda r} : 1 \leqslant \lambda \leqslant L\}$ are calculated. The standard deviation is assigned as a systematic uncertainty of the fit for the given r.

The method is expanded to multiple data sets by generating independent Gaussian random variables for each data set. In principle, more complex correlations of uncertainties for an individual data set can be decoded in ρ_{ij}; however, for the data at hand these correlations are not known and thus cannot be implemented.

One can choose as the final y value for a given r either the mean from the data-shuffling method or the fit result of the original data (i.e., the fit result when the Gaussian variables are zero). The difference between them is usually negligible.

[1] E. V. Shuryak, Phys. Lett. B **78**, 150 (1978).
[2] A. Adare *et al.* (PHENIX Collaboration), Phys. Rev. Lett. **104**, 132301 (2010).
[3] A. Adare *et al.* (PHENIX Collaboration), Phys. Rev. C **91**, 064904 (2015).
[4] A. Adare *et al.* (PHENIX Collaboration), Phys. Rev. Lett. **123**, 022301 (2019).
[5] J. Adam *et al.* (ALICE Collaboration), Phys. Lett. B **754**, 235 (2016).
[6] G. Agakichiev *et al.*, Eur. Phys. J. C **4**, 249 (1998).
[7] L. Altenkämper, F. Bock, C. Loizides, and N. Schmidt, Phys. Rev. C **96**, 064907 (2017).
[8] A. Adare *et al.* (PHENIX Collaboration), Phys. Rev. C **81**, 034911 (2010).
[9] R. Hagedorn and J. Ranft, Nuovo Cimento Suppl. **6**, 169 (1968).
[10] S. Acharya *et al.* (ALICE Collaboration), Eur. Phys. J. C **78**, 263 (2018).
[11] B. Abelev *et al.* (ALICE Collaboration), Phys. Lett. B **717**, 162 (2012).
[12] S. Adler *et al.* (PHENIX Collaboration), Phys. Rev. C **75**, 024909 (2007).
[13] S. Acharya *et al.* (ALICE Collaboration), Eur. Phys. J. C **77**, 339 (2017).
[14] A. Adare *et al.* (PHENIX Collaboration), Phys. Rev. D **83**, 032001 (2011).
[15] S. Acharya *et al.* (ALICE Collaboration), Eur. Phys. J. C **78**, 624 (2018).
[16] S. Adler *et al.* (PHENIX Collaboration), Phys. Rev. Lett. **91**, 241803 (2003).
[17] T. Sjostrand, P. Eden, C. Friberg, L. Lonnblad, G. Miu, S. Mrenna, and E. Norrbin, Comput. Phys. Commun. **135**, 238 (2001).
[18] C. Rasmussen and C. Williams, *Gaussian Processes for Machine Learning* (MIT Press, Cambridge, MA, 2005).

[19] M. Bonesini *et al.* (WA70 Collaboration), Z. Phys. C **42**, 527 (1989).

[20] L. Apanasevich *et al.* (Fermilab E706 Collaboration), Phys. Rev. D **68**, 052001 (2003).

[21] C. Aidala *et al.* (PHENIX Collaboration), Phys. Rev. C **98**, 054903 (2018).

[22] U. Acharya *et al.* (PHENIX Collaboration), Phys. Rev. C **102**, 064905 (2020).

[23] A. Adare *et al.* (PHENIX Collaboration), Phys. Rev. C **87**, 034911 (2013).

[24] S. Acharya *et al.* (ALICE Collaboration), Phys. Rev. C **98**, 044901 (2018).

[25] J. Adam *et al.* (ALICE Collaboration), Eur. Phys. J. C **77**, 33 (2017).

[26] A. Adare *et al.* (PHENIX Collaboration), Phys. Rev. C **93**, 024901 (2016).

[27] B. Abelev *et al.* (ALICE Collaboration), Phys. Rev. Lett. **110**, 032301 (2013).

[28] K. Aamodt *et al.* (ALICE Collaboration), Phys. Rev. Lett. **106**, 032301 (2011).

[29] A. Adare *et al.* (PHENIX Collaboration), Phys. Rev. C **88**, 024906 (2013).

[30] J. Adam *et al.* (ALICE Collaboration), Phys. Rev. C **93**, 034913 (2016).